PHYSICAL REVIEW B VOLUME 58, NUMBER 15 15 OCTOBER 1998-I

Defect-mediated elastic resonances in He-atom scattering from single-crystal surfaces

A. L. Glebov* and J. P. Toennies
Max-Planck-Institut für Strömungsforschung, Bunsenstraße 10, D-37073 Göttingen, Germany

J. G. Skofronick
Department of Physics and MARTECH, Florida State University, Tallahassee, Florida 32306

J. R. Manson
Department of Physics and Astronomy, Clemson University, Clemson, South Carolina 29634

(Received 27 March 1998)

Experimental evidence for a new atom-surface resonant mechanism involving surface defects is presented. After an initial selective adsorption trapping into surface bound states of a NaCl(001) surface, He atoms are subsequently scattered from surface defects back into the continuum. The inverse process also occurs: He atoms scatter from a defect and some of the amplitude enters the bound state eventually followed by selective desorption from the bound state via diffraction. For the 90°-scattering geometry used, the resonances show up as sharp peaks in the angular distributions of the quasielastic intensity between the diffraction peaks and are symmetric about the specular peak. A general description of the process is given which shows that it is a universal feature of any scattering system which can exhibit selective adsorption type resonances.
[S0163-1829(98)00639-0]

I. INTRODUCTION

Single-crystal surfaces are characterized by a multitude of different imperfections such as vacancies, steps, kinks, dopants, adsorbates, and interstitials, all which can strongly influence epitaxial growth, diffusion during growth, chemical reactivity, and the way surfaces interact with their environment. Surface defects have been studied for several decades, providing an advanced level of understanding of the structures and properties of the defects as well as their formation mechanisms (see Ref. 1 and references therein). Generally, some defects on surfaces are expected under thermodynamic equilibrium and, additionally, surface preparation methods can also generate a number of diverse defects on surfaces of crystals.[2] Defects localized in the bulk[3–6] can segregate to the surface of the crystal and some types of defects produced on the surface can also diffuse into the interior. Surface defect structures may also exert a controlling influence on the interaction of atoms and molecules with surfaces.

Several spectroscopic studies of defects on ionic crystal surfaces have been conducted in the 1970s.[7,8] As early as the 1960s and 1970s, some experiments[9,10] were undertaken to study the structures of macroscopic surface defects such as steps on alkali halides by means of the metal decoration technique.[11] The studies demonstrated a strong dependence of the surface morphology on the surface preparation method. Using this technique Höche *et al.*[10] studied the effect of annealing on the NaCl(001) surface morphology and demonstrated that at surface temperatures around 470 K the surface steps round off and, therefore, lead to a reduction of the surface defect density. A detailed atomic force microscope (AFM) investigation of the step structures of differently cleaved NaCl(001) surfaces as well as their modifications with time upon various exposures has been recently reported.[12]

AFM images from alkali-halide surfaces with atomic resolution were first reported in 1990 by Meyer *et al.* for LiF(001) (Ref. 13) and NaCl(001).[14] Recently, a new noncontact mode of the AFM scanning allowed Lüthi *et al.*[15,16] to observe direct images of single defects on the surface of NaCl with atomic resolution at room temperature. However, it is still not feasible to obtain AFM images with atomic resolution at temperatures substantially higher or lower than 300 K. Moreover, an investigation of defect distributions, their mobilities, and interactions with atoms and molecules is not currently possible by this technique.[16]

In contrast, various types of surface imperfections can be extensively investigated by diffraction techniques. The effect of defects on diffraction is manifest in the modifications of both Bragg-diffraction peak intensities as well as contributions to the background intensities in the form of incoherent diffuse elastic and inelastic scattering. It has been shown that the surface defects can be most accurately characterized through a careful analysis of the weak background intensities of scattered helium atoms[17–20] or electrons[21,22] between the diffraction peaks. In particular, defects on the surface introduce rather large perturbations of the electron density, for which very low surface coverage densities can be sensitively probed by atom scattering.

Three main classes of surface defects can be studied separately in diffraction experiments according to their spatial dimensions:[19,23] (1) zero-dimensional or point defects (adsorbed particles, vacancies, interstitial atoms and/or ions, substitutions of atoms and/or ions); (2) one-dimensional defects (steps, kinks, stacking faults, dislocations); (3) two-dimensional defects (surface domains, ordered clusters of point defects such as adsorbate islands, terraces of different heights). The intensity distributions as functions of parallel momentum transfer $\Delta\mathbf{K}=\mathbf{K}_f-\mathbf{K}_i$ of the atoms scattered from different types of surface defects were discussed in detail, for instance, by Choi *et al.*,[24] by Cowley,[23] and also by Wöll and Lahee.[19] For the scattering from randomly distributed *isolated* steps or point defects, for which the structure factor $S(\mathbf{k},\omega)$ is a constant proportional to the surface cov-

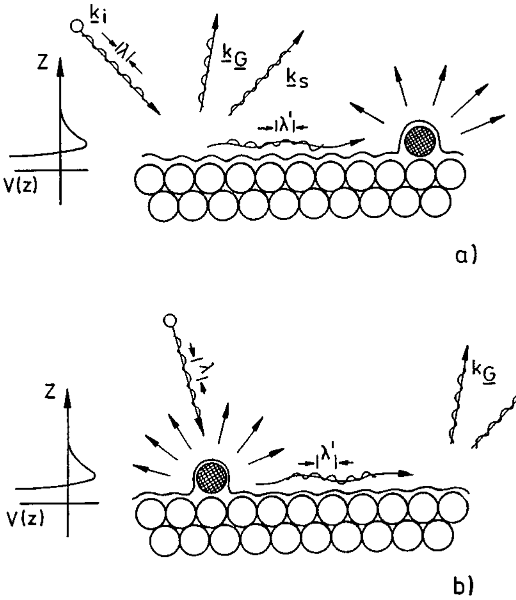

FIG. 1. Schematic representation of the direct (a) and time-reversed (b) processes that contribute to diffuse elastic resonances. Scattering into the specular and Bragg diffraction channels are marked with $\mathbf{k}_S$ and $\mathbf{k}_G$, respectively. In (a) the defect scatters back out into the continuum that part of the wave that was initially diffracted into the bound state, while in (b), the defect scatters part of the incident wave into the bound state from which it subsequently leaves via a diffraction process.

erage density Θ, the intensity distribution can be expressed in terms of the form factor $I(\Delta\mathbf{K}) \propto \Theta|\tau_{fi}|^2$, where $|\tau_{fi}|^2$ is the form factor, which is the scattering amplitude from a single defect.[25]

Recently we reported[26] evidence that surface defects are also involved in either trapping the incident He atoms into a bound state or scattering of the atoms already in the surface bound state back into the continuum. These are called defect-mediated elastic resonances (DER). In the surface scattering apparatus with a fixed source-detector angle, the DER features show up as pairs of peaks of roughly equal intensity symmetrically positioned about the specular peak.[26] This symmetry can be easily explained using Fig. 1, which is a schematic drawing of the basic processes leading to DER phenomenon. For example, Fig. 1(a) shows a mechanism in which a portion of the incoming beam can diffract (selectively adsorb) into one of the bound states, but subsequently encounters a defect while in the bound state. At the initial collision vertex shown in the figure, the incident beam is scattered into the specular peak ($\mathbf{k}_S$) as well as into all the available open diffraction channels ($\mathbf{k}_G$). Simultaneously, the part of the beam diffracted into a bound state is constrained to move along the surface. The wave amplitude traveling in the bound state can then collide with a symmetry-breaking defect, which allows it to scatter back out into the continuum in all directions. Thus, this resonant scattering mechanism manifests itself as an enhanced intensity in the diffuse elastic background at all final angles whenever the initial beam meets the conditions for selective adsorption into one of the bound states. The kinematic conditions for selective adsorption resonances are summarized in Appendix A. A compilation of the known measured and theoretically calculated values of the bound state energies of ^{4}He-NaCl used in this work are listed in Table I.

Figure 1(b) depicts the inverse process in which a beam incident at a given angle on the surface collides with a symmetry-breaking defect. The defect scatters amplitude in all directions, but in addition it may scatter amplitude into one of the bound states. For that part of the wave trapped in the bound state, the most likely mechanism to escape back into the continuum is through a selective desorption process.

TABLE I. Table of bound-state levels used in this work for the bound-state energies in the He-NaCl(001) interaction potential, together with a list of bound state values from other experiments and calculations.

$-\epsilon_0$ (meV)	$-\epsilon_1$	$-\epsilon_2$	$-\epsilon_3$	$-\epsilon_4$	Ref.
		Experimental Values			
	3.35		0.30		Present work, 26
7.21±0.10		1.62±0.07	0.41±0.12		27
	3.7±0.4				28, 29
	3.4±0.1				30
7.1±0.05					31
	4.1±0.1	1.5±0.1	0.31±0.05		32, 33
		Calculated Values			
	4.08	1.46	0.4		34
	4.09	1.55	0.47		34
	4.18	1.64	0.48	0.08	35
	4.02	1.51	0.41	0.07	35
	3.82	1.41	0.38		36
	4.02	1.51	0.41		36
7.17	3.64	1.43	0.29		37
8.4	4.1	1.5	0.31		38
	3.7				39

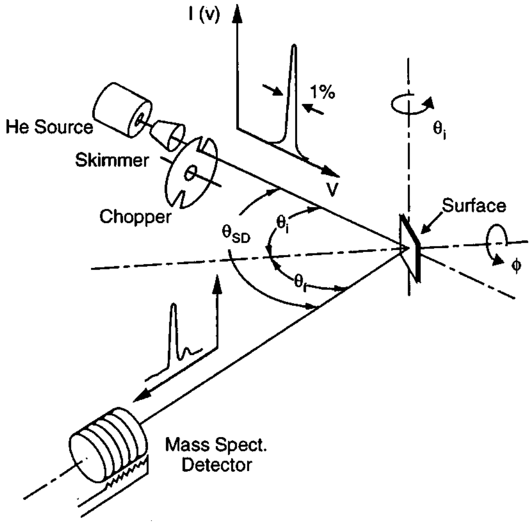

FIG. 2. Schematic view of the experimental arrangement showing the incident (Θ_i) and final (Θ_f) angles along with the main components of the instrument. The vacuum system consists of four main chambers containing: (1) the He source with the 10-μm-diameter nozzle, and skimmer; (2) chopper; (3) target; and (4) detector. In addition, the apparatus contains five differential pumping stages between these four main chambers.

Thus, this mechanism causes an enhancement of the diffuse elastic intensity in those directions for which the final scattered beam satisfies bound state resonance conditions, for any arbitrary incident angles and energies.

The present article extends the DER studies that we presented in Ref. 26. It provides a detailed description of the measurement technique that has been used to separate out the diffuse elastic signal from the other inelastic terms for investigations of DERs. This article also presents experimental results on the DER's obtained in the [110] direction of the NaCl(001) surface, and provides additional inelastic helium-atom scattering (HAS) data for the NaCl(001)[100] direction. In addition, in this work we present a method involving the difference between angular distributions before and after annealing that makes it possible to reveal DER features without time-of-flight (TOF) energy analysis.

The article is organized in the following way. The next section describes the experimental apparatus. Section III presents the experimental results of observations of DER in the two high symmetry directions of the NaCl(001) crystal face. Section IV describes the effect of surface annealing on the DER resonances. Section V provides a summary of the results along with a discussion of possibilities for future experiments. In Appendixes A and B the kinematic conditions of selective adsorption resonances are presented together with the theoretical description of the resonance peak line shapes.

II. APPARATUS

The helium-atom scattering (HAS) apparatus is shown schematically in Fig. 2 and described briefly below. Additional technical details have been given previously.[40,41] A highly monoenergetic He beam (full width at half maximum $\Delta v/v<1\%, \Delta E/E<2\%$) was produced by a supersonic expansion through a 10-μm aperture into vacuum. The beam was then chopped, and after scattering from the crystal surface, the He atoms were detected at a distance of 147 cm from the target by an ionizer and mass spectrometer operating in a single-ion counting mode. The angle between incoming and outgoing beams is fixed at $\Theta_{SD}=\Theta_i+\Theta_f=90.1°$, where Θ_i and Θ_f are the incident and final scattering angles measured with respect to the surface normal. Different momentum transfers ΔK parallel to the surface are accessed by a polar rotation of the sample around an axis perpendicular to the sagittal plane and for elastic scattering are given by $\Delta K=k_i(\sin\Theta_f-\sin\Theta_i)$, where k_i is the incident wave vector. In the measurements reported here the incident energies ranged from about 10 to 29 meV, corresponding to wave vectors of 4.4 to 7.5 Å^{-1}, respectively. Measurements were taken in the [100] and [110] directions, the two major symmetry azimuths of the fcc (001) surface.

The NaCl crystal target[42] used in this work was cleaved in vacuum at scattering chamber pressures near the mid-10^{-11}-torr range. It had a nearly square face with edges 6–7 mm^2 long of which only about a 3-mm-diameter area was illuminated by the incident He-atom beam. Prior to the cleave, the target chamber was baked to about 425 K for about 15 h. During measurements the crystal was cooled by a liquid-helium cold finger, which was coupled to the sample holder by means of an oxygen-free high-conductivity (OFHC) braid. The crystal was radiatively heated by a filament mounted immediately behind the sample holder. The crystal temperature was measured by a NiCr/Ni thermocouple located in a small hole drilled into the side of the crystal. Most of the experiments presented in this work were conducted at crystal temperatures between 70 and 100 K. At these temperatures and at the residual gas pressure of less than 5×10^{-11} torr, adsorption of contaminations on the surfaces is very small and the crystal remains clean for several days. At room temperature maintained between measurements, the contaminants desorb from the surface.

The manipulator allowed the surface of the crystal to be aligned into the proper orientation by permitting translation in the x, y, and z directions, azimuthal rotation, and adjustment of the angle of tilt. The entire manipulator was mounted on a differentially pumped rotary feedthrough so that the polar scattering angle could be adjusted without disturbing the other alignment angles of the crystal.

III. EXPERIMENTAL RESULTS

A. Measuring method

In order to study the diffuse elastic scattering of atoms from surface defects, the elastic signal was distinguished from the inelastic contributions by the time-of-flight technique for each set of incident and final angles to produce elastic angular distributions (EAD). The technique is illustrated in Fig. 3 for He atoms with an incident wave vector $k_i=6.55$ Å^{-1} scattering from the NaCl(001) surface along the [100] azimuth. Figure 3(a) shows an overview of the total scattering intensity angular distribution (AD) obtained by rotating the target so as to change the incident and final scattering angles Θ_i and Θ_f, respectively. The major diffraction peaks corresponding to the surface reciprocal lattice vectors (1,1), (2,2), $(\overline{1},\overline{1})$, and $(\overline{2},\overline{2})$ have intensities of about

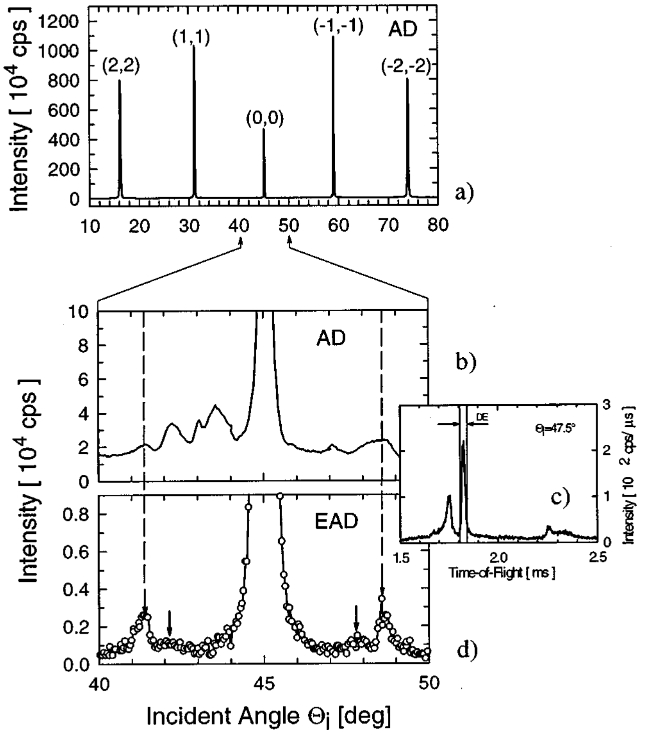

FIG. 3. Angular distributions of He atoms, with wave vector $k_i = 6.55$ Å^{-1}, incident on the NaCl(001) surface in the [100] surface azimuth. (a) shows the total angular distribution (AD). The diffraction peak intensities are labeled in parentheses. (b) shows an expanded view of the AD at angles ±5° away from the specular peak showing the total diffuse intensity. (c) shows a TOF spectrum taken at the same incident wave vector and $\Theta_i = 47.5°$ with the diffuse elastic window marked. Only the particles within this window are counted in an EAD. (d) shows the elastic angular distribution (EAD). The arrows mark the peaks for the diffuse elastic resonances. The resonances appear symmetrically positioned about the specular angle.

10^7 counts/sec (cps) whereas the specular peak has only about 6×10^6 cps. The diffraction peaks have a full width at half maximum (FWHM) of about 0.02 Å^{-1}. This corresponds to the surface coherence length[43] of approximately 300 Å, which is comparable to the transfer width of the apparatus and indicates the typical good long-range order routinely obtained for alkali-halide cleaved surfaces.

The angular region ±5° on both sides of the specular peak is shown with an enlarged intensity scale in Fig. 3(b). The many features seen are mostly due to single phonon assisted inelastic resonances and focusing effects discussed previously.[30,44–50] These peaks are mixed with the directly scattered inelastic intensity from single phonon creation and annihilation events and have an average intensity of about 2×10^4 cps. In order to determine the diffuse elastic signal, TOF spectra were measured at angular intervals of 0.1°. A representative TOF spectrum taken at $k_i = 6.55$ Å^{-1} and $\Theta_i = 47.5°$ is shown in Fig. 3(c). The peak at zero energy transfer, associated with the diffuse *elastic* scattering from surface defects, is clearly separated from the inelastic single phonon features. The elastic energy window varied from about 0.4 to 1 meV around the elastic peak depending on the energy of the incident beam. Figure 3(d) presents the elastic angular distribution (EAD) of the intensity in the elastic energy window. The EAD reveals a number of sharp structures marked with vertical arrows (↓), which are identified as the defect-mediated elastic resonance (DER) features. Note that the DER peaks are symmetrically positioned about the specular peak with a somewhat uniform background intensity of less than 10^3 cps. Often in the experiments reported here the DER signals are as small as 5×10^2 cps on a background of roughly equal intensity. Thus, it is clear that a detector dynamical range of 4–5 orders of magnitude is necessary for observing these resonant features.

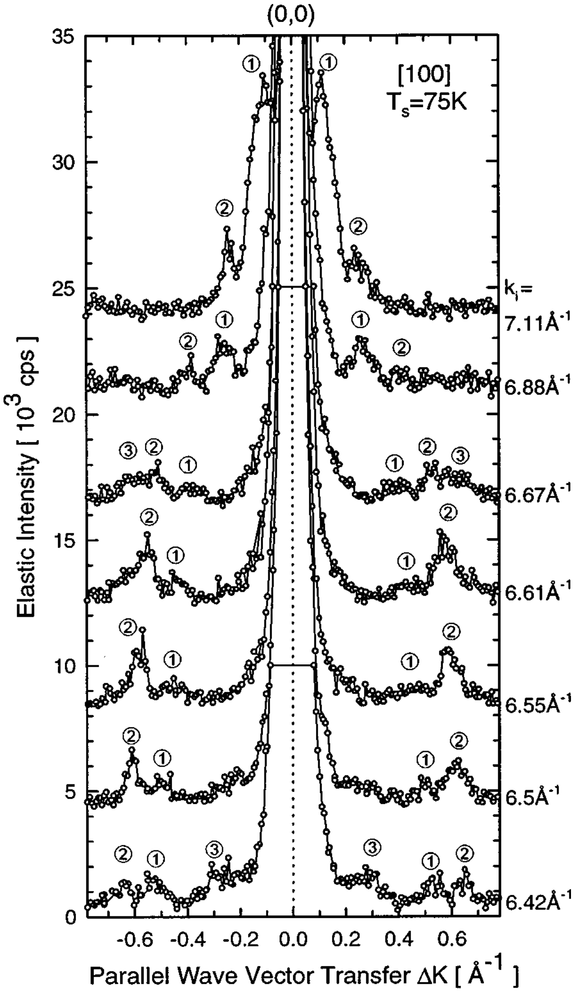

FIG. 4. A selected sequence of typical EAD measurements of the diffuse elastic intensity as a function of parallel wave vector transfer ΔK for He incident on NaCl(001) in the [100] surface azimuthal direction at seven different incident wave vectors $k_i = 6.42–7.11$ Å^{-1}. The peaks marked with numbers are the diffuse elastic resonance features. The numbers 1, 2, and 3 denote the $(1,1)_3$, $(2,0)_1$, and $(-2,2)_3$ resonances, respectively.

B. Results on NaCl(001)[100]

Extensive measurements of the EAD's were carried out in both the [100] and [110] azimuthal directions of the NaCl(001) surface. The measurements along the [100] direction will be presented first. In this direction, the EAD's were measured for 13 different incident wave vectors ranging from $k_i = 5.09$ to 6.0 Å^{-1}. Figure 4 shows representative EAD's at seven different incident wave vectors k_i. As men-

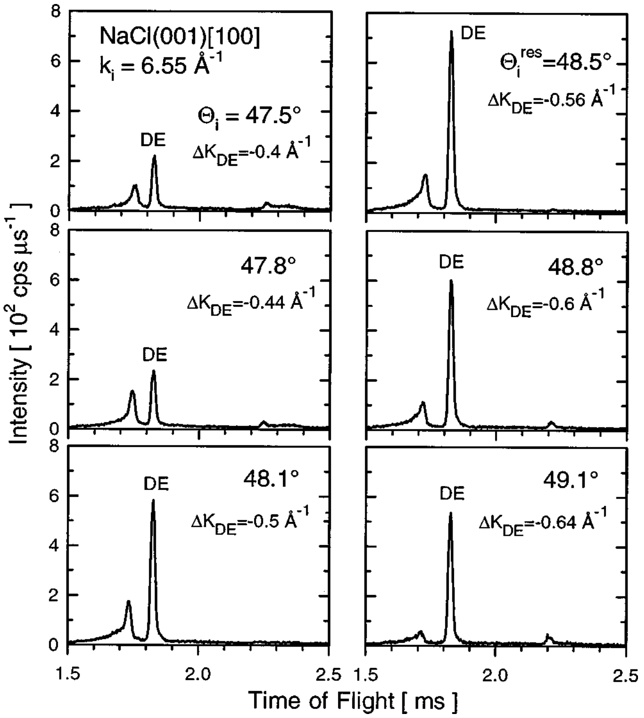

FIG. 5. Time-of-flight spectra measured in the vicinity of peak 2 at $\Delta K = -0.56$ Å^{-1} from the EAD spectrum at $k_i = 6.55$ Å^{-1} shown as the third curve from the bottom in Fig. 4. The incident angles Θ_i and the parallel wave vector transfers for the corresponding diffuse elastic peaks ΔK_{DE} are presented. The sharp increase of the diffuse elastic peak at $\Theta_i = 48.5°$ corresponds to a maximum of the DER peak 2 in the EAD.

tioned above, low surface temperatures are favorable for the resonance measurements and, therefore, in the present case the temperature was kept at $T_s = 75$ K. In each of the scans two to three DER features, denoted by 1, 2, and 3, are symmetrically positioned about the specular peak ($\Delta K = 0$) and the intensity of each symmetric pair is nearly equal as explained in detail in connection with Eq. (B1) in Appendix B. The DER peaks are quite narrow as expected for resonance features, and comparable in FWHM to the diffraction peaks.

The observed peaks are not diffraction features, which might be caused by an unexpected periodic superstructure arrangement on the surface. If the peaks were diffractive in origin they would appear at constant positions in ΔK regardless of the incident total wave vector. Instead they show a marked shift in ΔK for different incident k_i and, therefore, can be unambiguously attributed to bound-state resonance features.

Using a notation $(G_x, G_y)_n$, where n is the number of the bound state in the He-NaCl interaction potential, and G_x and G_y are the x and y components of $\mathbf{G}$ expressed in units of the NaCl surface reciprocal lattice vector $\mathbf{G}_0 = 1.58$ Å^{-1}, the peaks in Fig. 4 will be identified as belonging to the $(1,1)_3$, $(2,0)_1$, and $(-2,2)_3$ resonances. It should be mentioned that the $(2,0)_1$ and $(-2,2)_3$ resonances are degenerate with the $(0,2)_1$ and $(2,-2)_3$, respectively. It is interesting to note that the positions of the two resonances $(1,1)_3$ and $(2,0)_1$ move toward smaller values of parallel wave-vector transfer $\mathbf{\Delta K}$ (smaller values of incident angle Θ_i) with increasing energy while the $(-2,2)_3$ resonance exhibits opposite behavior and moves to larger values of $\mathbf{\Delta K}$.

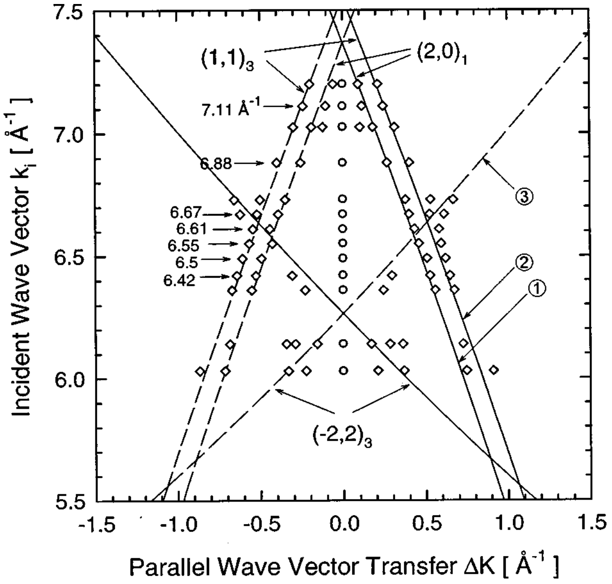

FIG. 6. Plot of the peak positions in total incident wave vector k_i as a function of parallel momentum transfer ΔK for He-atom scattering on NaCl(001) in the [100] azimuth. The data points shown as diamonds are the DER features, while the specular peak is marked with circles. The calculated curves show the expected positions of the DER features as predicted by Eq. (A1). The numbers 1, 2, and 3 denote the $(1,1)_3$, $(2,0)_1$, and $(-2,2)_3$ resonances, respectively.

In order to demonstrate that no inelastic processes are involved in the resonances under study, Fig. 5 shows the TOF spectra obtained at six different angles in the vicinity of peak 2 at $\Delta K \approx -0.56$ Å^{-1} of the EAD measured at $k_i = 6.55$ Å^{-1} presented in Fig. 4. For the spectrum measured in the out-of-resonance condition at $\Theta_i = 47.5°$, the intensity of the diffuse elastic peak (labeled by DE) is about 2×10^2 cps/μs. However, as the angle increases, moving closer and closer to the resonance position at $\Theta_i = 48.5°$, the diffuse elastic peak increases and reaches a maximum at the resonance position. Here the intensity of the diffuse elastic peak is more than 7×10^2 cps/μs, clearly demonstrating an increase by approximately a factor of 4. Upon further increase of the incident angle, the intensity of the diffuse elastic peak decreases again. In addition to the diffuse elastic peaks, all spectra contain several smaller phonon peaks. The phonon peaks are much more pronounced on the negative ΔE of the diffuse elastic peak, which corresponds to the phonon creation processes. Since the TOF measurements were performed at $T_s = 75$ K, this is easily understood in terms of the Bose-Einstein occupation factors,[51] which define the probability for phonon creation events to be much higher at this low temperature. Note that no significant changes of the phonon peak intensities are observed at the resonance condition. This provides additional evidence that inelastic phonon scattering processes do not contribute to DER.

In Fig. 6 the open diamond shaped data points show the positions of all observed DER peaks obtained from 13 EAD's in a plot of parallel wave-vector transfer $\mathbf{\Delta K}$ versus incident wave vector k_i and the circles show the position of the specular diffraction peak. The positions of the peaks cor-

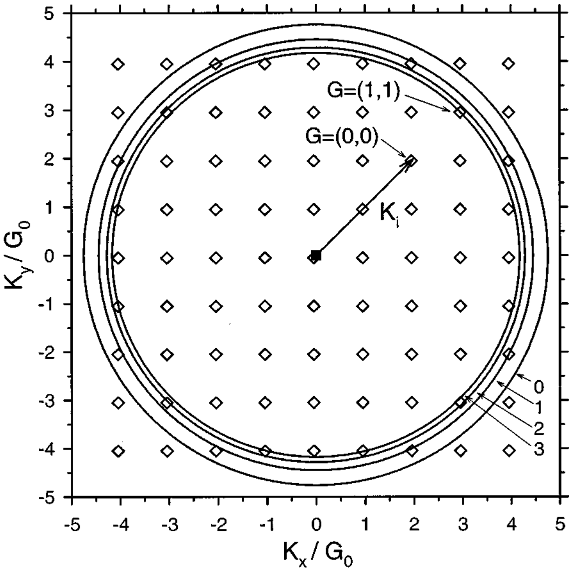

FIG. 7. The two-dimensional Ewald construction for He atoms incident on NaCl(001)[100] with a total wave vector $k_i = 6.55$ Å^{-1} and an incident angle $\Theta_i = 41.77°$. The origin indicated by the filled square is the starting point of the parallel projection of the incident wave vector $\mathbf{K}_i$. The diamonds are the reciprocal lattice points, the straight line is the incident parallel wave vector, and the large circles mark the radii of the four bound states for NaCl. In this example the ϵ_3 bound state is in resonance with the $\mathbf{G} = (1,1)$ reciprocal lattice vector, which is in the scattering plane. All wave vectors have been normalized to $\mathbf{G}_0 = 1.58$ Å^{-1}.

responding to the incident wave vectors of the seven EAD's presented in Fig. 4 are denoted by the horizontal arrows marked with the k_i values. Again, the DER peaks are clearly symmetrically positioned about $\Delta\mathbf{K} = 0$ and, as opposed to the constant $\Delta\mathbf{K}$ positions of the specular diffraction peak, two of the DER peaks (marked 1 and 2) move to smaller values of $|\Delta\mathbf{K}|$ with increasing incident energy, while the other peak (marked 3) moves in the opposite direction. The DER peaks cannot be confused with diffraction peaks, not shown in the figure, since the diffraction peaks do not shift with changing incident energy.

The nature of the resonances associated with the DER peaks in Fig. 6 can been seen in a two-dimensional Ewald plot (for the kinematics of the resonant atom-surface scattering see Appendix A). An example is shown in Fig. 7 for He incident on NaCl(001)[100] with a total wave vector $k_i = 6.55$ Å^{-1} and an incident angle $\Theta_i = 41.77°$ ($\Delta K \sim 0.6$ Å^{-1}). Those conditions correspond to peak 2 in the third from the bottom EAD panel in Fig. 4. The surface Ewald construction (e.g., see Ref. 52) is a plot of ΔK_x versus ΔK_y with the incident parallel momentum vector $\mathbf{K}_i$, drawn starting from the origin ($K_x, K_y = 0$) which is indicated by the squares in Fig. 7. A grid of reciprocal lattice points of NaCl(001) is placed with the $\mathbf{G} = (0,0)$ point at the head of the vector $\mathbf{K}_i$. Note that in the case presented, the $\mathbf{G} = (-2,-2)$ vector by chance nearly coincides with the origin of the graph. All those reciprocal lattice points which lie within a circle of radius k_i, with center at the origin (tail of $\mathbf{K}_i$) correspond to values of $k_{\mathrm{G}z}^2 > 0$ satisfying the condition for open diffraction channels and, therefore, are allowed diffraction peak positions. Reciprocal lattice points outside the radius k_i circle are evanescent diffraction states or in other words closed diffraction channels. The big circles shown in Fig. 7 are of radius $\sqrt{k_i^2 + 2m|\epsilon_n|/\hbar^2}$, corresponding to the bound state resonance conditions given by Eq. (A1) in Appendix A. Thus, reciprocal lattice points that fall exactly on one of the circles are in resonance with the incident beam. Figure 7 shows clearly that for the incident conditions shown, $k_i = 6.55$ Å^{-1} and $\Theta_i = 41.77°$, the ϵ_3 bound state is in resonance with the $\mathbf{G} = (1,1)$ reciprocal lattice vector. This is in agreement with Fig. 6, where peak 2 at $k_i = 6.55$ Å^{-1} lies on the resonance curve $(1,1)_3$. Similar Ewald-construction analysis of the other peaks observed in the EAD's measured for various incident wave vectors makes it possible to conclusively relate all of the peaks to the corresponding bound states and $\mathbf{G}$ vectors.

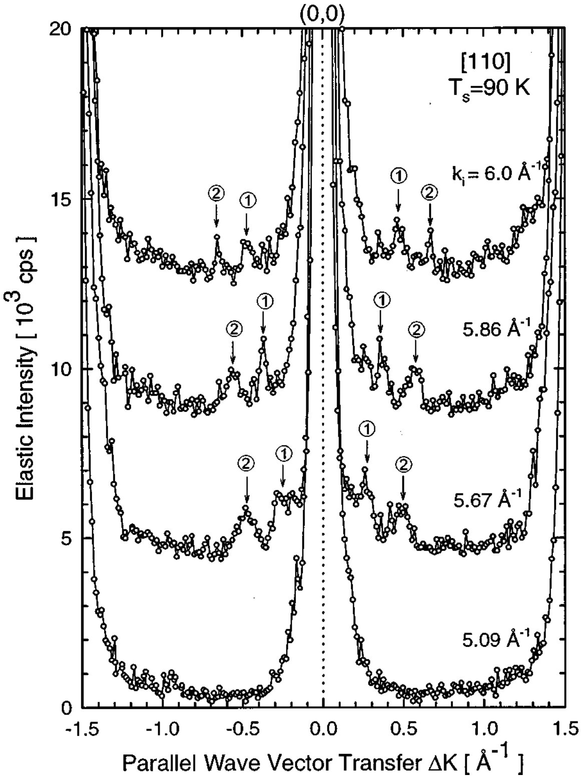

FIG. 8. EAD measurements of the diffuse elastic intensity as a function of parallel wave vector transfer $\Delta\mathbf{K}$ for He incident on NaCl(001) in the [110] surface azimuthal direction. Four different incident energies are shown, ranging from $k_i = 5.09$ to 6.0 Å^{-1}. The peaks marked with arrows (↓) are the DER features. For identification of the resonances see Fig. 9.

C. Results on NaCl(001)[110]

An extensive study of the defect-mediated diffraction resonances has also been carried out in the [110] azimuthal direction. In this direction the EAD's were measured for 10 different incident wave vectors ranging from $k_i = 5.09$ to 6.3 Å^{-1}. Figure 8 shows four panels of EAD measurements giving the elastic intensity as a function of parallel momentum exchange for values of the incident wave vector $k_i = 5.09$, 5.67, 5.86, and 6.0 Å^{-1}. The measurements were performed at the crystal temperature of 90 K. Aside from the EAD at $k_i = 5.09$ Å^{-1}, all the others have two pairs of peaks

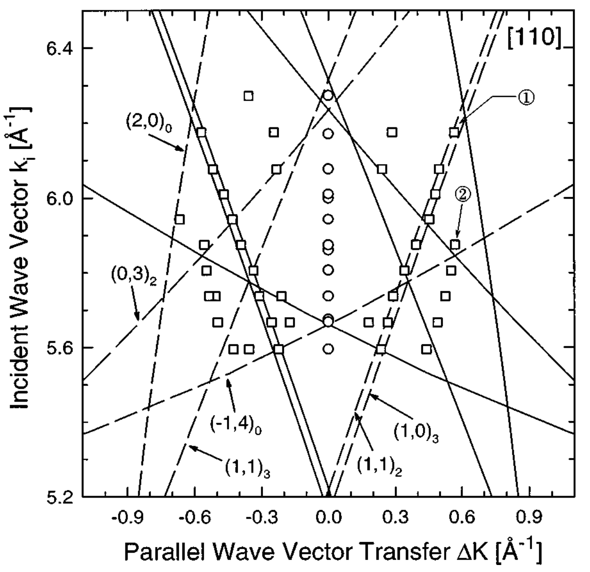

FIG. 9. Plot of the peak positions of total incident wave vector as a function of parallel momentum exchange for He-atom scattering on NaCl(001)[110]. The data points shown as squares are the DER features, while the specular peak position is represented by circles. The solid and dashed lines show the expected positions of the DER features as predicted by Eq. (A1).

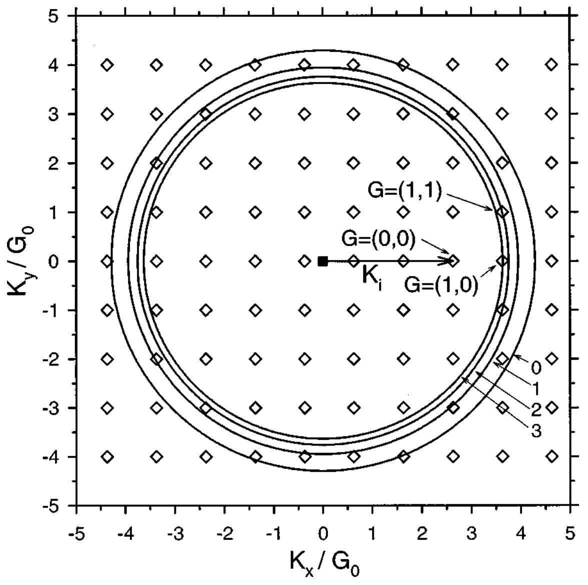

FIG. 10. The two-dimensional Ewald construction for He incident on NaCl(001)[110] with a total wave vector $k_i = 5.67$ Å^{-1} and an incident angle $\Theta_i = 46.97°$, related to peak 1 at $\Delta K = -0.27$ Å^{-1} in the corresponding EAD from Fig. 8. The diamonds are the reciprocal lattice points, the straight line is the incident parallel wave vector, and the circles mark the radii of the four bound states. In this example the ϵ_3 bound state is in resonance with the $\mathbf{G} = (1,0)$, and the ϵ_2 bound state is in a symmetric double resonance with the $\mathbf{G} = (1,\pm 1)$ reciprocal lattice vector.

that are associated with DER's. The DER features are small, sharp peaks near the specular, which are marked by vertical arrows (↓) and the numbers 1 and 2. As in Fig. 4 for the [100] directions, the DER peaks are symmetrically positioned around the specular peak and the intensity of each symmetric pair is nearly equal.

Identification of the DER peaks observed in the [110] direction is more complicated than in the [100] case. This is illustrated in Fig. 9. Two series (labeled 1 and 2) of measured DER peaks are indicated by open squares; they show a linear shift to larger $\Delta\mathbf{K}$ values with increasing incident energy. The solid line curves are the locus of points of the bound state resonance condition, calculated with Eq. (A1) for the incident beam with selected bound states. The dashed curves are for resonance conditions in the final beam direction.

As seen from Fig. 9, there are two resonance curves $(1,1)_2$ and $(1,0)_3$, which are aligned along the line of measured data points marked by 1 in Fig. 9. An important point is that the uncertainties in the bound-state energies (Table I) may be as large as ±3% and this can lead to a corresponding uncertainty in the position of the resonance curves. Even such a shift of both resonance curves does not permit the fitting of the data points from the series 2 in Fig. 9. There are also several data points around $\Delta K \pm 0.3$ Å^{-1} and $k_i \sim 6.2$ Å^{-1} that cannot be exactly fitted with the bound states from Table I. As an example, the nature of the resonance associated with the DER peak 1 from the EAD measured at $k_i = 5.67$ Å^{-1} and shown in Fig. 8 (second from the bottom) is presented in the two-dimensional Ewald plot of Fig. 10. Figure 10 shows that for the incident conditions $k_i = 5.675$ Å^{-1} and $\Theta_i = 46.97°$, the ϵ_3 bound state is in resonance with the $\mathbf{G} = (1,0)$ reciprocal lattice vector, since the ϵ_3 circle crosses the corresponding $\mathbf{G} = (1,0)$ point in the reciprocal space. Furthermore, the ϵ_2 bound state circle in Fig. 9 crosses symmetrically two reciprocal lattice vectors $\mathbf{G} = (1,\pm 1)$ and, thus, is in a symmetric double resonance with these two vectors.

This is precisely the situation observed in Fig. 9. The loci of points for the $(1,0)_3$ and the $(1,\pm 1)_2$ resonances are very close and parallel to each other. This double resonance passes through all of the points of the DER 1 series nearest to specular for the negative values of $\Delta\mathbf{K}$. The same resonances applied to the outgoing beam in the detector direction correspond to the symmetrical mirror image peaks on the opposite side of the specular beam, as shown by the dashed line in Fig. 9. There are several other resonance curves shown, always with solid curves used to show solutions of Eq. (A1) for resonance conditions with the incident beam and dashed curves to show resonance conditions with the final beam.

Interestingly, none of the combinations of the bound state energies ϵ_n and the $\mathbf{G}$ vectors provides a resonance curve that fits the loci of the measured series 2 peaks of Fig. 9. There are several possible reasons for this. First, as mentioned above, there is a substantial uncertainty in the values of the bound state energies as seen in Table I. However, this alone is not enough to explain the data. Second, the exact dynamical expression describing the resonance is the Feshbach-Fano amplitude of Eq. (B5), which allows for a shift in position of the resonance energy given by $-\mathrm{Re}\, h_{bb}$ as in Eq. (B7). In fact, Vargas and Mochan[39] demonstrated that such band-structure effects might shift the measured energy of the lowest bound state of He-NaCl by up to 10% (~0.5 meV) to lower energies, with a somewhat smaller shift expected for the higher energy bound states. A shift of the bound-state energy for one of the resonance curves ($(1,0)_3$ or $(1,\pm1)_2$) in Fig. 9 within just 5 to 10% from the value used here (see Table I) would fit well the measured data points of series 2, and thus explain the nature of this resonance.

A third possibility that may help to explain the observed data points would be splitting of the calculated bound-state curves $(1,0)_3$ and $(1,\pm1)_2$ due to quantum mechanical interference effects[25] resulting from the proximity of these resonances in the $(\Delta K,k_i)$ space (see Fig. 9). In the case of two bound states participating simultaneously in the scattering process the transition matrix [Eq. (B5) in Appendix B] must be rewritten to include the projection of two resonances, which leads to

$$T_{fi}=h_{fi}+\frac{h_{fb}h_{bi}(E_i-E_{b'}-h_{b'b'})+h_{fb'}h_{b'i}(E_i-E_b-h_{bb})+h_{fb}h_{bb'}h_{b'i}+h_{fb'}h_{b'b}h_{bi}}{(E_i-E_b-h_{bb})(E_i-E_{b'}-h_{b'b'})-h_{bb'}h_{b'b}}, \tag{1}$$

where h_{bb} and $h_{b'b'}$ are the self-energy terms for two simultaneously resonant bound states labeled b and b', and $h_{bb'}$ and $h_{b'b}$ are the coupling terms between these bound states. Setting the denominator of the second term on the right-hand side of Eq. (1) equal to zero gives the familiar expression for the lifting of the degeneracy in energy for a pair of degenerate quantum states when they are coupled by a perturbation. Equation (1) contains not only energy shifts of the resonance positions given by Re h_{bb} and Re $h_{b'b'}$, it also shows a splitting of the two bound-state energies through the term $h_{bb'}h_{b'b}$. The combination of energy shift and splitting could be sufficient to move one of the resonant loci curves [$(1,0)_3$ or $(1,\pm1)_2$] to the position of the series of peak 2 positions. An alternative possibility would arise if the shift were sufficiently large that it caused the (1,0) or $(1,\pm1)$ to be in resonance with a different bound state at the positions of the peak 2 series.

IV. ANNEALING OF THE DEFECTS

To check that indeed intrinsic defects of NaCl are involved, the surface defect density was intentionally reduced by baking the NaCl crystal for 12 h at a temperature of 500 K. In the 1970s Höche *et al.*[10] demonstrated that the density of the surface defects can be significantly reduced by annealing the NaCl crystal at $T_s=470$ K predominantly through the rounding of the steps. Later, in the 1990s, HAS studies of the NaCl(001) surface topography[53,54] showed that the quality of a NaCl surface destroyed by vacuum UV photon stimulated desorption could be recovered upon extensive annealing at $T_s>450$ K. Figure 11 depicts two pairs of total (top panels) and elastic (bottom panels) angular distributions. On the left side of Fig. 11 the AD and EAD measured from the NaCl(001)[100] surface at $T_s=90$ K immediately after cleavage are shown. The maximum diffraction peak intensities in the AD (top left) are about 6×10^6 counts/s, while the diffuse elastic background intensity in the corresponding EAD (bottom left) is about 2×10^4 cps. Several DER peaks are clearly seen in the EAD with the strongest ones reaching the intensity of $\approx6\times10^4$ cps. These two most intense DER features are marked by vertical arrows. On the right side of Fig. 11, the AD and EAD measured from the same surface after annealing at $T_s=500$ K for 12 h are shown. The measurements before and after annealing were performed at the same surface temperature and crystal adjustment.

The magnification of the background signals, observed in the AD's (top panels of Fig. 11) before and after annealing, are exhibited in Figs. 12(a) and 12(b), respectively. Since the angular distributions presented in Figs. 11, 12(a), and 12(b) were measured at the same surface temperature and beam conditions, the intensity values can also be directly compared. The overall effect of the annealing can be summarized as follows:

(1) After annealing, the Bragg diffraction peak intensities increased by 30–50% (compare the left and right plots on the top panel of Fig. 11) and the widths of the peaks become narrower. For example, the width of the first-order diffraction peak before annealing comprised 0.22°, while after annealing it became 0.17°.

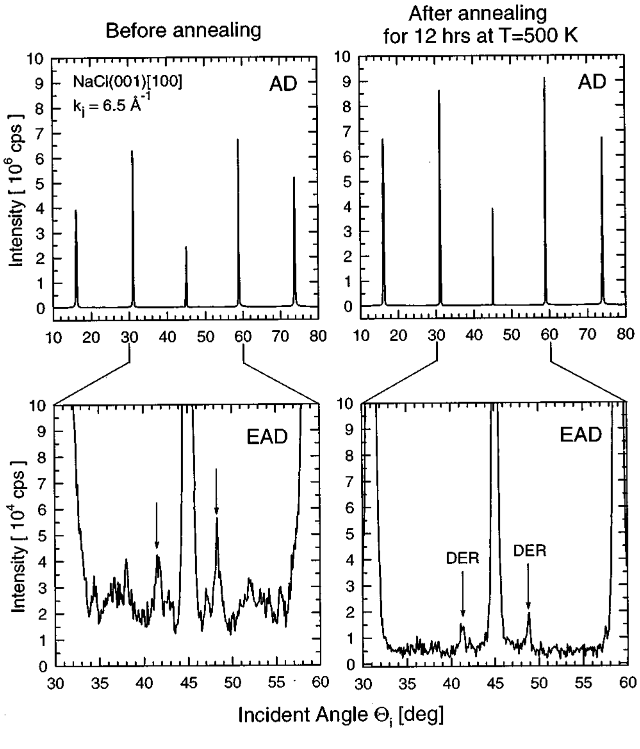

FIG. 11. The total (top panel) and elastic (bottom panel) angular distributions from the NaCl(001) surface along the [100] direction, measured at $k_i=6.5$ Å^{-1} and $T_s=90$ K. On the left side, the AD and EAD are presented from a NaCl surface cleaved *in situ*, whereas the angular distributions on the right side were measured on the same surface under the same conditions after additional annealing of the crystal at $T_s=500$ K for 12 h.

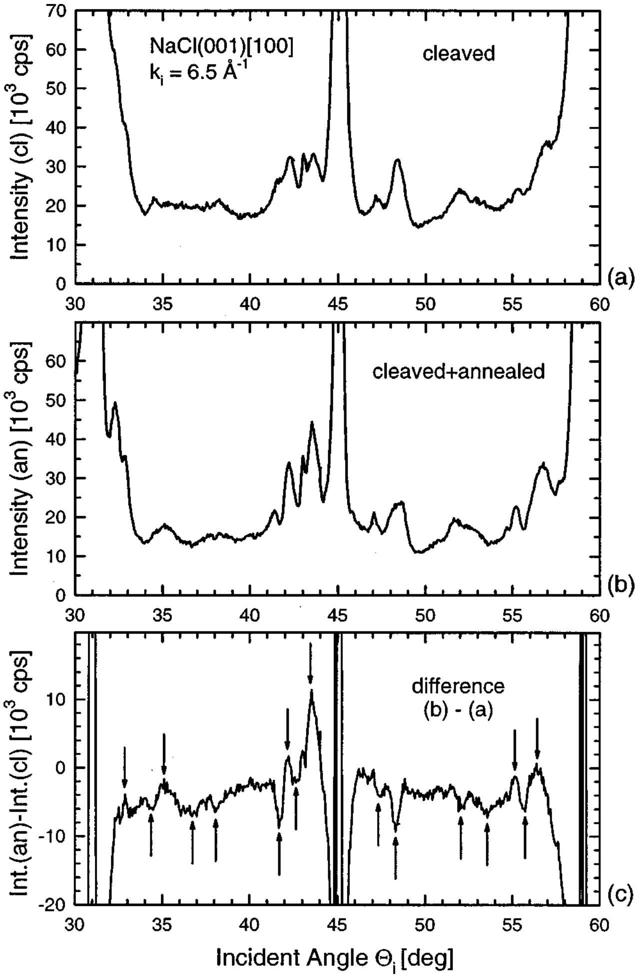

FIG. 12. (a) The magnification of the total background signal from the preceding Fig. 11 (top left panel) measured on the cleaved but *not* annealed NaCl(001) surface in the [100] azimuth. (b) The magnification of the total background signal from Fig. 11 (top right panel) measured on the NaCl(001) surface that was cleaved *and* then annealed at 500 K for 12 h. (c) The difference between the background intensities, obtained after (a) was subtracted from the (b) signal. The downward directed arrows (↓) mark the phonon-assisted processes, while the upward directed arrows (↑) mark those associated with the DER's.

(2) The diffuse elastic background signal after annealing is decreased by approximately a factor of 4 and similarly for the signal from the DER peaks (left and right plots on the bottom panel of Fig. 11). As is clearly seen from the figure, some of the smaller DER peaks observed in the EAD measured from the nonannealed surface disappear after this temperature treatment.

(3) A redistribution of the total background intensity upon annealing is apparent from the total angular distributions of Figs. 12(a) and 12(b). In addition to the overall decrease of the background, some of the resonance peaks increase, while the others show a significantly less intense signal. As will be discussed below, this can be attributed to different contributions from inelastic and diffuse elastic scattering processes to the background intensity.

The increased intensities and the reduced widths of the Bragg diffraction peaks are clearly indicative of the improvement in short- and long-range order on the surface. This may be attributed to both rounding of the step edges[10] and removal of the surface point defects. The decrease of the diffuse elastic background strongly suggests the lowering of the density of the surface defects as well. In addition to the total background, the smoothing of the surface upon annealing resulted in a dramatic decrease of the DER peak intensities. This provides evidence that the resonances observed in the present work are mediated by intrinsic surface defects.

This analysis of the redistributed total background intensities upon annealing reveals a method for distinguishing the resonances involving defects and those involving surface phonons through the use of difference spectra. Figure 12(c) plots the intensity difference in the background signals before and after annealing on the surface [the intensity of Fig. 12(a) is subtracted from the intensity of Fig. 12(b)]. First of all, it is evident that the subtraction of the two spectra reduces the total background by about $(3-5)\times 10^3$ cps. In addition there are a number of peaks [phonon-assisted peaks marked by (↓)] and dips [DER features marked by (↑)] that are prominent in the background profile. The dips can be attributed to DER features, since their intensity decreases upon annealing (see Fig. 11). On the other hand, the probability for a particle to interact with surface phonons upon either entering or leaving a bound state becomes higher with a decrease of the surface defect density. This results in the corresponding increase of the surface coherence length, and to sharper and more intense phonon-assisted resonance peaks in Fig. 12(c). Therefore, in this manner the peaks in the angular distributions, related to phonon-assisted selective adsorption resonances, can be easily separated from pure elastic DER features without the need for TOF energy resolution.

V. CONCLUSIONS AND FUTURE POSSIBILITIES

A new mechanism for resonance scattering of particles from surfaces has been identified and investigated experimentally for He atoms scattered from the NaCl(001) surface, along the two high symmetry azimuthal directions [100] and [110]. The process involves a coherent selective adsorption into one of the surface bound states followed by scattering from defects into the continuum. The inverse process has also been identified, where the particles impinging on the surface enter the bound state through the interaction with a surface defect followed by coherent diffractive scattering into the continuum. From the kinematics and symmetry properties it is shown that these two processes are time and parity reversal invariant.

The DER's are revealed by the observation of the following effects: (1) They obey the kinematical conditions of Eq. (A1) dictated by the reciprocal lattice vectors $\mathbf{G}_{m,n}$ participating in the scattering process together with the bound-state energy levels ϵ_n (see Figs. 6 and 9). This indicates that one of the scattering channels (exit or entry) involves a selective adsorption resonance with a bound state of the interaction potential. (2) The resonance peaks appear in the diffuse elastic background between the large diffraction peaks indicating that surface defects are involved in the scattering process (see Figs. 4 and 8). (3) The peaks appear as pairs of nearly equal intensity and shape and they are symmetrically positioned about the specular peak as imposed by the time-reversal symmetry of the transition matrix as established in Eq. (B1). (4) Annealing of the surface defects leads to significant reduction of the DER peak intensities (see Figs. 11 and 12). The intensity of the DER peaks is large compared to the background because the partial wave in one of the bound states of the potential is constrained to a two dimensional wave close to and parallel to the surface and the probability of encountering a defect is therefore greatly enhanced. Thus, the scattering into the bound state ‘‘compresses’’ the incoming 3D plane wave into a 2D wave traveling parallel to the surface. As the experiments demonstrate, the scattering cross section of surface defects for the 2D wave propagating in a bound state on the surface gives an enhanced intensity signal as compared to the initial 3D plane wave colliding on the surface.

There are a number of interesting implications of the DER effect.

(1) The quantitative study of DER peaks will allow the measurements of the differential and total cross sections of defects on the surface under extraordinarily well-defined conditions as a result of illumination by the two-dimensional incident wave in different selected bound states. This configuration contrasts with the usual case in which a defect is illuminated by an incident three-dimensional plane wave. In order to measure the complete differential cross section, the detector would have to be able to move independently of the incident beam, that is not possible in the present apparatus.

(2) The analysis of bound states using DER’s provides significant constraints on the energy values of the bound states and thus should be useful in confirming or perhaps identifying new states in atom/molecule-surface interaction potentials.

(3) The DER effect provides a way of studying a fundamental and important question of quantum mechanics such as: What is the nature of a 2D plane wave? In the bound state, the wave has the unique characteristic that its probability amplitude is constrained in the normal direction to lie within a very few Å of the surface, while it spreads significantly in the other two directions. Thus, the wave has well-defined momentum only in the directions parallel to the surface, however, because it is ‘‘attached’’ to the incident plane wave outside of the surface it has a very well defined total energy. The nature of the wave function in the bound state is similar to the well-known Andreev two-dimensional surface states of ^{3}He on the surface of ^{4}He.[55] The DER effect provides a way to test the nature of the 2D waves in the bound states through the incoherent collisions of the trapped particles with the defects.

(4) The DER features can be revealed without the need for TOF energy analysis by subtracting angular distributions measured with different defect coverages.

(5) There are some interesting possibilities for *inelastic* effects associated with DER. One possibility can be called a defect-mediated inelastic resonance (DIR) in which the particles gain or lose a quantum of energy when they scatter from the defect. For example, taking the case exhibited in Fig. 1(a), a particle could enter the bound state resonantly via a diffraction process and then subsequently collide *inelastically* and transfer a quantum of energy from a localized mode of the defect. The particles would be scattered into the continuum just as in a DER, however, simultaneously transferring the energy $\pm\hbar\omega$ of the localized defect mode. This process should be particularly important if the defect is a purposefully adsorbed atom or molecule with localized Einstein vibrational modes polarized parallel to the surface, such as frustrated translational modes. This is because simple models of inelastic scattering of atoms by phonons show that the interaction matrix element is proportional to the momentum (or impulse) transferred in the collision.[56] Since the particles traveling resonantly in the bound state have all of their translational momentum directed parallel to the surface this would tend to favor large parallel momentum transfers. Thus both the direct and time reversal DIR resonance processes should lead to significant and selective enhancement of the inelastic intensities which have been observed previously as due to the direct scattering by localized modes of very low coverage densities of adsorbates on the surface.[57]

(6) As was discussed in the Introduction, the $\Delta\mathbf{K}$ dependence differs significantly for the atoms scattered from various types of defects. Thus, measurement of the intensities of the DER peaks as a function of the incident beam energy, which leads to the shift of the peaks in $\Delta\mathbf{K}$ space, may open new possibilities to study separately and with higher sensitivity the interaction of different defect types with the particles colliding with the surface.

(7) The DER is not limited to atom or molecule scattering, it should also be observed in electron scattering, or any other scattering process where one can observe selective adsorption type resonances.[58,59]

ACKNOWLEDGMENTS

This research was supported in part by DOE Grant No. DE-FG02-97ER45635, NSF Grant No. DMR 9726229, and NATO Grant GRG.961145. J.R.M. and J.G.S. thank Professor J. P. Toennies and the Max-Planck-Institut für Strömungsforschung for their hospitality during part of this work.

APPENDIX A: KINEMATICS OF RESONANT ATOM-SURFACE SCATTERING

The expected positions of the selective adsorption resonances are readily calculated from the conservation of parallel momentum and total energy.[60–62] A plane wave incident on a rigid periodic surface with a wave vector $\mathbf{k}_i=(\mathbf{K}_i, k_{iz})$ has energy $E_i=\hbar^2k_i^2/2m$. Since the surface is periodic only in a direction parallel to the surface, the parallel momentum $\mathbf{K}$ is conserved modulo a surface reciprocal lattice vector $\mathbf{G}$, while the perpendicular momentum is not conserved. Thus the allowed diffraction scattering channels will have wave vectors given by $\mathbf{k}_{\mathbf{G}}=(\mathbf{K}_i+\mathbf{G}, k_{\mathbf{G}z})$ where the perpendicular component is determined by conservation of energy $k_{\mathbf{G}z}^2=k_i^2-(\mathbf{K}_i+\mathbf{G})^2$. Selective adsorption bound-state resonances occur whenever

$$k_{\mathbf{B}z}^2=k_i^2-(\mathbf{K}_i+\mathbf{B})^2=-2m|\epsilon_n|/\hbar^2, \qquad \text{(A1)}$$

where ϵ_n is the energy of the nth bound state in the surface adsorption well and $\mathbf{B}$ is one of the $\mathbf{G}$ vectors. Under the conditions of Eq. (A1), direct diffraction into the bound state is energetically allowed and the wave function has an amplitude component that is constrained to a bound state of the surface potential in the normal direction but parallel to the surface has a shorter wavelength than the incident wave. Equation (A1) also gives the conditions on the incident beam for observing the direct DER resonance of Fig. 1(a) in which the He initially diffracts into the bound state and then is diffusely scattered out of the bound state by subsequent scattering by a defect. For the inverse DER process of Fig. 1(b), the beam of total wave vector k_i is incident at any arbitrary angle and the portion of the amplitude that is scattered into a bound state by a defect subsequently exits the bound state via a diffraction process. The discrete diffraction channels in which this additional intensity is observed in the outgoing scattered waves is again given by a condition similar to Eq. (A1) except with $\mathbf{K}_i$ replaced by $\mathbf{K}_f$. This, then, explains why the DER features are observed as pairs symmetrically positioned about the specular peak. With the fixed source-detector geometry employed here, interchanging the incident angle Θ_i with the final angle Θ_f is equivalent to interchanging $\mathbf{K}_i$ with $\mathbf{K}_f$.

APPENDIX B: DER LINE SHAPES AND INTENSITIES

The observed intensities of pairs of symmetric DER features can be shown to result from parity and time-reversal invariance. It is evident from Fig. 3, and also from Figs. 4 and 8, that the intensities of the symmetric pairs of peaks are nearly equal for all values of the incident total wave vector. This can be easily explained in terms of the scattering matrix. The scattering matrix is invariant under time-reversal and parity inversion of the potential (TP invariance), which implies that for even-parity surface potentials the two DER mechanisms of Figs. 1(a) and 1(b) are time-reversed images of each other. In particular, for even parity surfaces, which is the case for (001) surfaces of fcc crystals, we have the following equality in the transition matrix:

$$\langle \mathbf{k}_f | T | \mathbf{k}_i \rangle = e^{i\gamma} \langle \mathbf{k}_s | T | \mathbf{k}_{f'} \rangle, \tag{B1}$$

where T is the transition operator, $\mathbf{k}_s$ is the state specular to $\mathbf{k}_i$ and $\mathbf{k}_{f'}$ is the incident state whose specular is $\mathbf{k}_f$, i.e., $\mathbf{k}_f$ and $\mathbf{k}_{f'}$ differ only in that the perpendicular components of their momenta have opposite signs. The result of interchanging final and initial angles in this in-plane fixed angle experiment is not only to change $\Delta\mathbf{K}$ into $-\Delta\mathbf{K}$, but it is also the operation $\mathbf{k}_i \to \mathbf{k}_{f'}$ simultaneously with $\mathbf{k}_f \to \mathbf{k}_s$. This explains why for each value of k_i in Figs. 4 and 8, pairs of peaks are symmetrically located at $\pm\Delta\Theta$ on either side of the specular position at $\Theta_i = 45°$ (or equivalently, at $\pm\Delta\mathbf{K}$). For a surface with even parity, or simply even parity on average, the two symmetric peaks will have equal intensities.

Finally, the fact that the DER features appear as peaks in the intensity is discussed in terms of the dynamics of the scattering process. An appropriate theoretical formalism with which to describe these resonances is the method of Feshbach projection, which is often used to describe ordinary selective adsorption resonances.[63–67] The transition operator, which obeys the relation

$$T = V + VG_0T, \tag{B2}$$

where V is the interaction potential and G_0 is the Green function, can also be expressed by the pair of operator equations

$$T = h + hG_0^{(1)}T, \tag{B3}$$

$$h = V + VG_0^{(2)}h, \tag{B4}$$

where the Green function G_0 has now been split into two parts: $G_0^{(1)}$, which propagates only the resonant state (or small number of simultaneously resonant states), and $G_0^{(2)}$, which propagates all the rest of the nonresonant states.

For example, in the simplest case of a single isolated bound state resonance, the mechanism depicted in Fig. 1(b) results in a transition matrix for scattering from initial state $\mathbf{k}_i$ to final state $\mathbf{k}_f$ given by

$$\langle \mathbf{k}_f | T | \mathbf{k}_i \rangle \equiv T_{fi} = h_{fi} + h_{fb} \frac{1}{E_b - E_i - h_{bb}} h_{bi}, \tag{B5}$$

where an obvious shorthand notation is used for the matrix elements. In Eq. (B5) the leading term h_{fi} is the reduced transition matrix calculated from Eq. (B4) for scattering directly from $\mathbf{k}_i$ to $\mathbf{k}_f$ upon collision with the defect, while the second term describes the resonant path through the bound state b, i.e., h_{bi} is the reduced transition matrix for scattering from the initial state into the bound state, h_{fb} is the amplitude for scattering out of the bound state into the final state and h_{bb} is the self-energy of the bound state. The observed intensity is proportional to $|T_{fi}|^2$, and for the transition matrix of Eq. (B5) this gives an intensity that has a Fano line shape.[67] The condition for the resonance term in Eq. (B5) to dominate is

$$|h_{fi}| \ll |h_{fb}h_{bi}/\mathrm{Im}\ h_{bb}|, \tag{B6}$$

in which case the Fano line shape reduces to a single Lorenzian peak. For the example of Fig. 1(b), the reduced matrix element h_{fb} comes from a diffraction process and is expected to be large, whereas h_{fi} and h_{bi} are expected to have small moduli because they result from scattering by the defect, and furthermore $\mathrm{Im}\, h_{bb}$ is also expected to be small (i.e., $\hbar/\mathrm{Im}\, h_{bb}$ is the lifetime of a particle in the resonant bound state, which is expected to be long compared to a direct collision time). Thus, these arguments imply that the condition of Eq. (B6) will be satisfied for the mechanism of Fig. 1(b), and consequently this resonance feature should appear as a sharp Lorenzian peak. By extension, Eq. (B1) implies that the resonance appearing symmetrically on the opposite side of the specular peak corresponding to the process depicted in Fig. 1(a) will also have the same line shape and intensity.

As a final point, it is noted that the position of the bound state feature can be best assigned to the position at which the real part of the Green function denominator of Eq. (B5) vanishes:

$$E_b - E_i - \mathrm{Re}\ h_{bb} = 0. \tag{B7}$$

This condition is equivalent to Eq. (A1) except now the energy of the bound state is shifted by an amount $-\mathrm{Re}\, h_{bb}$. This shows that the kinematical resonance condition of Eq. (A1) is only an approximate result, and the true resonance position can be shifted if the real part of the self-energy Re h_{bb} is significant.

---

*Present address: Bell Laboratories, Lucent Technologies, Murray Hill, New York 07974-0636.

[1] M. Henzler, W. Göpel, and C. Ziegler, *Oberflächenphysik des Festkörpers* (Teubner, Stuttgart, 1994).

[2] J. Lapujoulade, in *Interaction of Atoms and Molecules with Solid Surfaces*, edited by V. Bortolani, N. H. March, and M. P. Tosi (Plenum Press, New York, 1990), p. 381.

[3] K. S. Song and R. T. Williams, *Self-Trapped Excitons*, Springer Series in Solid-State Sciences Vol. 105 (Springer-Verlag, Berlin, 1993).

[4] F. Agullo-Lopez, C. R. A. Catlow, and P. D. Townsend, *Point Defects in Materials* (Academic Press, London, 1988).

[5] M. I. Klinger, C. B. Lushchik, T. B. Mashovets, G. A. Kholodar, M. K. Sheinkman, and M. A. Elango, Usp. Fiz. Nauk. **147**, 523 (1985). [Sov. Phys. Usp. **28**, 994 (1985)].

[6] N. Itoh, Adv. Phys. **31**, 491 (1982).

[7] V. M. Bermudez, Surf. Sci. **74**, 568 (1978).

[8] J. T. Hare and O. S. Heavens, J. Phys. C **10**, 4211 (1977).

[9] H. Berthge, G. Kaester, and M. Krohn, Z. Naturforsch. A **16a**, 321 (1961).

[10] H. Höche and H. Berthge, J. Cryst. Growth **33**, 246 (1976).

[11] H. Berthge, M. Krohn, and H. Stenzel, in *Electron Microscopy in Solid State Physics*, edited by H. Berthge and J. Heydenreich, Materials Science Monographs Vol. 40 (Elsevier, Amsterdam, 1987).

[12] H. Weiss, Habilitation Thesis, University of Hannover, 1995.

[13] E. Meyer, H. Heinzelbaum, H. Rudin, and H. J. Güntherodt, Z. Phys. B **79**, 3 (1990).

[14] G. Meyer and N. M. Amer, Appl. Phys. Lett. **56**, 2100 (1990).

[15] R. Lüthi, E. Meyer, M. Bammerlin, A. Baratoff, J. Lue, M. Guggisberg, C. Gerber, L. Howald, and H. J. Güntherodt, Z. Phys. B **100**, 165 (1996).

[16] R. Lüthi, M. Bammerlin, and E. Meyer, Phys. Bl. **53**, 435 (1997).

[17] A. M. Lahee, J. R. Manson, J. P. Toennies, and C. Woell, Phys. Rev. Lett. **57**, 471 (1986).

[18] A. Lock, B. J. Hinch, and J. P. Toennies, in *Kinetics of Ordering and Growth at Surfaces*, edited by M. G. Lagally (Plenum Press, New York, 1990).

[19] C. Wöll and A. M. Lahee, in *Helium Atom Scattering from Surfaces*, edited by E. Hulpke, Springer Series in Surface Science Vol. 27 (Springer-Verlag, Berlin, 1992).

[20] A. T. Yinnon, D. A. Lidar, I. Farbman, R. B. Gerber, P. Zeppenfeld, M. A. Krzyzowski, and G. Comsa, J. Chem. Phys. **106**, 4228 (1997).

[21] M. Henzler, in *Electron Spectroscopy for Surface Analysis*, edited by H. Ibach (Springer-Verlag, Berlin, 1977).

[22] K. Heinz, D. K. Saldin, and J. B. Pendry, Phys. Rev. Lett. **55**, 2312 (1985).

[23] J. M. Cowley, *Diffraction Physics* (North-Holland, Amsterdam, 1981), Chap. 7, p. 139.

[24] B. H. Choi, K. T. Tang, and J. P. Toennies, J. Chem. Phys. **107**, 9437 (1997).

[25] J. R. Manson, in *Helium Atom Scattering from Surfaces*, edited by E. Hulpke, Springer Series in Surface Science Vol. 27 (Springer-Verlag, Berlin, 1992), p. 173.

[26] A. Glebov, J. R. Manson, J. G. Skofronick, and J. P. Toennies, Phys. Rev. Lett. **78**, 1508 (1997).

[27] G. Benedek, G. Brusdeylins, R. B. Doak, J. G. Skofronick, and J. P. Toennies, Phys. Rev. B **28**, 2104 (1983).

[28] H. Hoinkes, Rev. Mod. Phys. **52**, 933 (1980).

[29] J. R. Bledsoe, Research Laboratories for the Engineering Sciences Report No. AEEP-3719-101-72U, 1972 (unpublished).

[30] G. Benedek, R. Gerlach, A. Glebov, G. Lange, S. Miret-Artes, J. G. Skofronick, and J. P. Toennies, Phys. Rev. B **53**, 11 211 (1996).

[31] G. Benedek, A. Glebov, W. Silvestri, J. G. Skofronick, and J. P. Toennies, Surf. Sci. Lett. **381**, L540 (1997).

[32] W. Y. Leung, J. Z. Larese, and D. R. Frankl, Surf. Sci. Lett. **143**, 398 (1984).

[33] D. R. Frankl, *Progress in Surface Science* (Pergamon, New York, 1983), Vol. 13, p. 285.

[34] F. O. Goodman and M. C. Vargas, Surf. Sci. **176**, 619 (1986).

[35] D. Eichenauer and J. P. Toennies, Surf. Sci. **197**, 267 (1988).

[36] J. M. Hutson and P. W. Fowler, Surf. Sci. **173**, 337 (1986).

[37] A. Frigo, F. Toigo, M. W. Cole, and F. O. Goodman, Phys. Rev. B **33**, 4184 (1986).

[38] S. Chung and M. W. Cole, Surf. Sci. **145**, 269 (1984).

[39] M. C. Vargas and W. L. Mochan, Surf. Sci. **355**, 115 (1996).

[40] A. Glebov, MPISF Report No. 14/1997, ISSN 0436-1199 (1997).

[41] J. P. Toennies and R. Vollmer, Phys. Rev. B **44**, 9833 (1991).

[42] Karl Korth Kristalle GmbH, Am Jägersberg 3, 24161 Altenholz, Germany.

[43] G. Comsa, Surf. Sci. **81**, 57 (1979).

[44] D. Evans, V. Celli, G. Benedek, J. P. Toennies, and R. B. Doak, Phys. Rev. Lett. **50**, 1854 (1983).

[45] G. Brusdeylins, R. B. Doak, and J. P. Toennies, J. Chem. Phys. **75**, 1784 (1981).

[46] G. Lilienkamp and J. P. Toennies, Phys. Rev. B **26**, 4752 (1982).

[47] G. Lilienkamp and J. P. Toennies, J. Chem. Phys. **78**, 5210 (1983).

[48] G. Benedek, Phys. Rev. Lett. **35**, 234 (1975).

[49] G. Benedek and S. Miret-Artes, Surf. Sci. Lett. **339**, 935 (1995).

[50] A. Glebov, J. R. Manson, S. Miret-Artes, J. G. Skofronick, and J. P. Toennies, Phys. Rev. B **57**, R9455 (1998).

[51] J. P. Toennies, in *Dynamics of Gas-Surface Interaction*, edited by G. Benedek and U. Valbusa, Springer Series in Chemical Physics Vol. 21 (Springer-Verlag, Berlin, 1982), p. 208.

[52] K. H. Rieder, in *Dynamics of Gas-Surface Interaction* (Ref. 51), p. 61.

[53] H. Höche, J. P. Toennies, and R. Vollmer, Phys. Rev. B **50**, 679 (1994).

[54] H. Höche, J. P. Toennies, and R. Vollmer, Phys. Rev. Lett. **71**, 1208 (1993).

[55] A. F. Andreev, Zh. Eksp. Teor. Fiz. **50**, 1415 (1966) [Sov. Phys. JETP **23**, 939 (1966)].

[56] J. R. Manson, Phys. Rev. B **43**, 6924 (1991).

[57] F. Hofmann and J. P. Toennies, Chem. Rev. **96**, 1307 (1996).

[58] E. G. McRae, Rev. Mod. Phys. **51**, 541 (1979).

[59] M. Rocca and F. Moresco, Phys. Rev. Lett. **73**, 822 (1994).

[60] J. E. Lennard-Jones and A. F. Devonshire, Nature (London) **137**, 1069 (1936).

[61] J. E. Lennard-Jones and A. F. Devonshire, Proc. R. Soc. London, Ser. A **156**, 6 (1936).

[62] J. E. Lennard-Jones and A. F. Devonshire, Proc. R. Soc. London, Ser. A **158**, 242 (1937).

[63] H. Feshbach, Ann. Phys. (N.Y.) **5**, 357 (1958).

[64] H. Feshbach, Ann. Phys. (N.Y.) **19**, 287 (1962).

[65] K. L. Wolfe and J. H. Weare, Phys. Rev. Lett. **41**, 1663 (1978).

[66] K. L. Wolfe and J. H. Weare, Surf. Sci. **84**, 581 (1980).

[67] N. G. V. Celli and J. Hutchinson, Surf. Sci. **87**, 112 (1979).